ADVANCED ENERGY & SUSTAINABILITY RESEARCH
www.advenergysustres.com

Field-Directed Growth of Hematite for Advanced Solar Hydrogen Production

*Fabio A. Pires, Touraj Karimpour, David Patrun, Thomas Fischer, Flavio L. Souza, and Sanjay Mathur**

Interplay of magnetic susceptibility and vapor phase nucleation in magnetic field-assisted chemical vapor deposition (mf-CVD) enables precise control over phase evolution, crystallographic orientation, and surface texturing in metal oxide thin films. The synthesis of hematite (α-Fe_2O_3) thin films via chemical vapor deposition using $[Fe_2(O^tBu)_6]$ as a molecular precursor is reported. Applying an external magnetic field (1 T) during deposition significantly alters the microstructure of the hematite films, reflected in superior photoelectrochemical (PEC) performance. Relative to zero-field deposition, mf-CVD increased the photocurrent density of hematite by 74%, attributed to magnetically induced texturing and densification, both enhancing charge separation and transfer efficiencies. Magnetic field-assisted hematite growth also increases the electrochemically active surface area, while a 33 mV photovoltage gain suggests a stronger built-in electric field in the α-Fe_2O_3-1 T film. Electrochemical impedance spectroscopy further confirms a reduced surface state density supporting improved interfacial charge dynamics. Furthermore, the magnetically altered material exhibits remarkable stability for 100 h of PEC operation. The results highlight hematite as a model photoanode for elucidating how magnetic fields modulate active domains in metal oxides, offering an innovative process to transform materials through applied fields.

1. Introduction

Chemical vapor deposition (CVD) is a continuous process with interlocked gas-phase and surface reactions.[1,2] With its broad parametric space and tunable chemical input through diverse molecular precursors, and high industrial relevance, CVD is a powerful model system for studying magnetic field influences on thin film growth. The interaction of magnetic fields ($\vec{B}$) with matter (e.g., Zeeman energy, magnetic torque, Lorentz and Faraday forces) can alter nucleation events and growth dynamics during magnetic field-assisted CVD (mf-CVD).[3–5] For instance, previous works show that the application of an external magnetic field can alter precursor flux during plasma-enhanced CVD, modulating the microstructure by inducing anisotropy in hematite (α-Fe_2O_3) grains.[6]

Furthermore, application of an external magnetic field during CVD induces a pronounced effect beyond phase control, yielding films with higher crystallinity, larger particulates, and enhanced out-of-plane magnetic anisotropy.[7] Using $Fe(CO)_5$ as a precursor, post-annealed hematite nanorods exhibited directional growth aligned with the magnetic field, indicating field-driven modulation of atomic diffusion and crystallization kinetics.[8] This consistent effect across various substrates highlights the versatility of mf-CVD for engineering anisotropic microstructures and tailored architectures.[9] Similarly, mf-CVD was found to alter the degree of inversion in the inverse spinel magnesium ferrite ($MgFe_2O_4$) films.[10] The technique has also been applied to tailor surface properties, texture, and phase purity in TiO_2 nanostructures grown from a paramagnetic Ti(III) precursor, expanding the concept of magnetically directed anisotropic growth.[11]

The structural control enabled by mf-CVD is expected to translate into functional gains, particularly in energy conversion applications. Hematite films produced via mf-CVD have consistently

F. A. Pires, T. Karimpour, D. Patrun, T. Fischer, S. Mathur
Institute of Inorganic and Materials Chemistry
University of Cologne
50939 Cologne, Germany
E-mail: sanjay.mathur@uni-koeln.de

The ORCID identification number(s) for the author(s) of this article can be found under https://doi.org/10.1002/aesr.202500313.

DOI: 10.1002/aesr.202500313

F. A. Pires, F. L. Souza
Brazilian Nanotechnology National Laboratory (LNNano)
Brazilian Center for Research in Energy and Materials (CNPEM)
13083-100 Campinas, Brazil

F. A. Pires, F. L. Souza
Institute of Chemistry
State University of Campinas (UNICAMP)
13083-970 Campinas, Brazil

F. L. Souza
Center for Natural and Human Sciences
Federal University of ABC (UFABC)
09210-580 Santo André, Brazil

exhibited superior photoelectrochemical (PEC) properties, yet key catalytic parameters remain insufficiently understood.[12,13] In this work, we provide a detailed investigation of PEC differences in samples grown under zero-field and applied-field conditions, with a focus on how magnetically modulated domains influence catalytic activity in complex ceramic systems.

A 74% enhancement in photocurrent density at 1.23 V vs. RHE (reversible hydrogen electrode) was observed for α-Fe_2O_3-1 T compared to the zero-field sample (α-Fe_2O_3-0 T). This improvement is attributed to higher charge separation and transfer efficiencies resulting in 21% increased photovoltage generation, and a larger electrochemically active surface area induced by the magnetic field-assisted growth. Electrochemical impedance spectroscopy (EIS) further reveals a reduced density of surface states in α-Fe_2O_3-1 T, indicating suppressed surface recombination and accelerated water oxidation kinetics. Finally, the field-induced growth of hematite yielded a photoanode with stability up to 100 h of PEC operation. These results highlight the ability of magnetic field-assisted CVD in modulating the structure and electronic properties of hematite, offering a general strategy for the catalytic design of metal oxides via magnetic-field-directed synthesis.

2. Results and Discussion

Thin films were produced by CVD of iron *tert*-butoxide ($Fe_2[O^tBu]_6$) precursor[14] and subsequent thermal treatment (550 °C, 1 h, air atmosphere). During CVD, film deposition onto fluorine-doped tin oxide (FTO) substrates was controlled with the aid of an external magnet. Samples without (α-Fe_2O_3-0 T) and with the influence of 1 T (α-Fe_2O_3-1 T) magnetic field were prepared, and a comprehensive PEC analysis was carried out to augment the knowledge on the effects of mf-CVD on catalytic materials properties.

2.1. Structural, Morphological, and Magnetic Properties

X-ray diffraction (XRD) technique (**Figure 1**a) showed patterns for α-Fe_2O_3-0 T and α-Fe_2O_3-1 T indexed to JCPDS card no. 33-0664, demonstrating that only the hematite phase (α-Fe_2O_3) of iron oxide was detected. Lotgering factors (F) calculated for α-Fe_2O_3-1 T exhibited preferential crystal growth for (110) crystallographic planes ($F = 0.69$) and decreased preference for (300) planes ($F = 0.22$) when compared to α-Fe_2O_3-0 T (see Table S1, Supporting Information), reinforcing the strong anisotropic effect of the magnetic field during the nanostructure growth. By changing the preferential crystal growth in the hexagonal hematite lattice (space group $R\bar{3}c$), grain densification at the [110] direction caused by mf-CVD suppressed (300) plane stacking (Figure 1b), influencing the preferential electronic conduction pathways. It is noteworthy that several studies associate increased anisotropy in the [110] direction with enhanced charge collection for hematite nanostructures grown onto FTO.[15] This is because tin dioxide has preferential growth vertically aligned to hematite's [110], favoring electron collection at the back contact.[16] Furthermore, bigger crystallite sizes observed for α-Fe_2O_3-1 T in the [110] direction (63.4 nm, see Table S2, Supporting Information) can be associated with magnetically induced saturation, consistent with hematite platelets exhibiting different density and roughness.[17]

High-resolution transmission electron microscopy (HRTEM) analysis highlighted the influence of the external magnetic field on nanostructure growth. Accessing localized cross-sectional information of the hematite films[18,19] revealed a predominance of highly verticalized grain growth for α-Fe_2O_3-1 T (Figure 1c), confirming the (110) crystal plane perpendicularly aligned to the substrate. On the other hand, α-Fe_2O_3-0 T (Figure 1d) grains did not present the same degree of verticalization compared to the magnetically altered sample. By monitoring the (110) plane, the perpendicular alignment was not found homogeneously for α-Fe_2O_3-0 T, corroborating the smaller preferential growth factor calculated from XRD analysis in this crystallographic direction. In addition, smaller grains observed for α-Fe_2O_3-0 T evidenced the magnetic saturation on grain growth and densification caused by mf-CVD.

Raman spectra (Figure 1e) showed further information on short-range hematite structural order, as characteristic vibrational modes were observed. For the centrosymmetric rhombohedral unit cell of hematite, all first-order phonon modes that are Raman allowed are infrared forbidden, and vice versa.[20,21] Predicted internal phonon modes related to the motion within a single $Fe(O)_6$ octahedral unit ($2A_{1g} + 3E_g$) and $2E_g$ external phonon modes, involving rotations and translations of entire Fe_2O_3 units were observed at 228 cm^{-1} (A_{1g}), 248 cm^{-1} (E_g), 296 cm^{-1} (E_g), 300 cm^{-1} (E_g), 416 cm^{-1} (E_g), 503 cm^{-1} (A_{1g}), and 615 cm^{-1} (E_g) for α-Fe_2O_3-0 T and α-Fe_2O_3-1 T.[21] Additionally, first and second-order bands are displayed at 667 cm^{-1} (1LO) and 1324 cm^{-1} (2LO), respectively. The first-order band is assigned to a Raman forbidden E_1 mode arising from the longitudinal optical (LO) branch.[21] The appearance of this mode has been attributed to disorder-induced breaking of hematite symmetry properties due to scattering of the LO phonon, commonly observed in the Raman spectra of polycrystalline, nanostructured, and doped hematite.[22] The most accepted assignment for the second-order band is a two-phonon scattering process, which is an overtone of the LO mode at 667 cm^{-1} and is thus referred to as the 2LO mode.[21] Broader peaks observed for α-Fe_2O_3-0 T, especially at the 1LO region, indicate a comparatively higher disorder degree in the crystalline structure of this sample, reinforcing the magnetic field aids in crystalline organization during the CVD process.

Additionally, X-ray photoelectron spectroscopy (XPS) was employed to investigate the chemical bonding of iron and its oxidation state. The full survey spectra, along with the high-resolution C 1s spectra used for calibration based on adventitious carbon, are provided in the supporting information (Figure S1, Supporting Information). High-resolution Fe 2p spectra (Figure 1f) of α-Fe_2O_3-0 T and α-Fe_2O_3-1 T exhibit the characteristic multiplet splitting into Fe $2p_{3/2}$ (725.3 and 725.5 eV, respectively) and Fe $2p_{1/2}$ (711.4 and 711.5 eV, respectively) components. In addition to the ≈14 eV separation of the doublets, the prominent satellite features shifted to higher binding energies confirm the dominant presence of Fe^{3+} species, as it is characteristic for shake-up processes in metallic high-spin configurations.[23] Although characterization so far points to the predominance of the hematite phase, the rise of divalent iron species at the surface of both samples can be

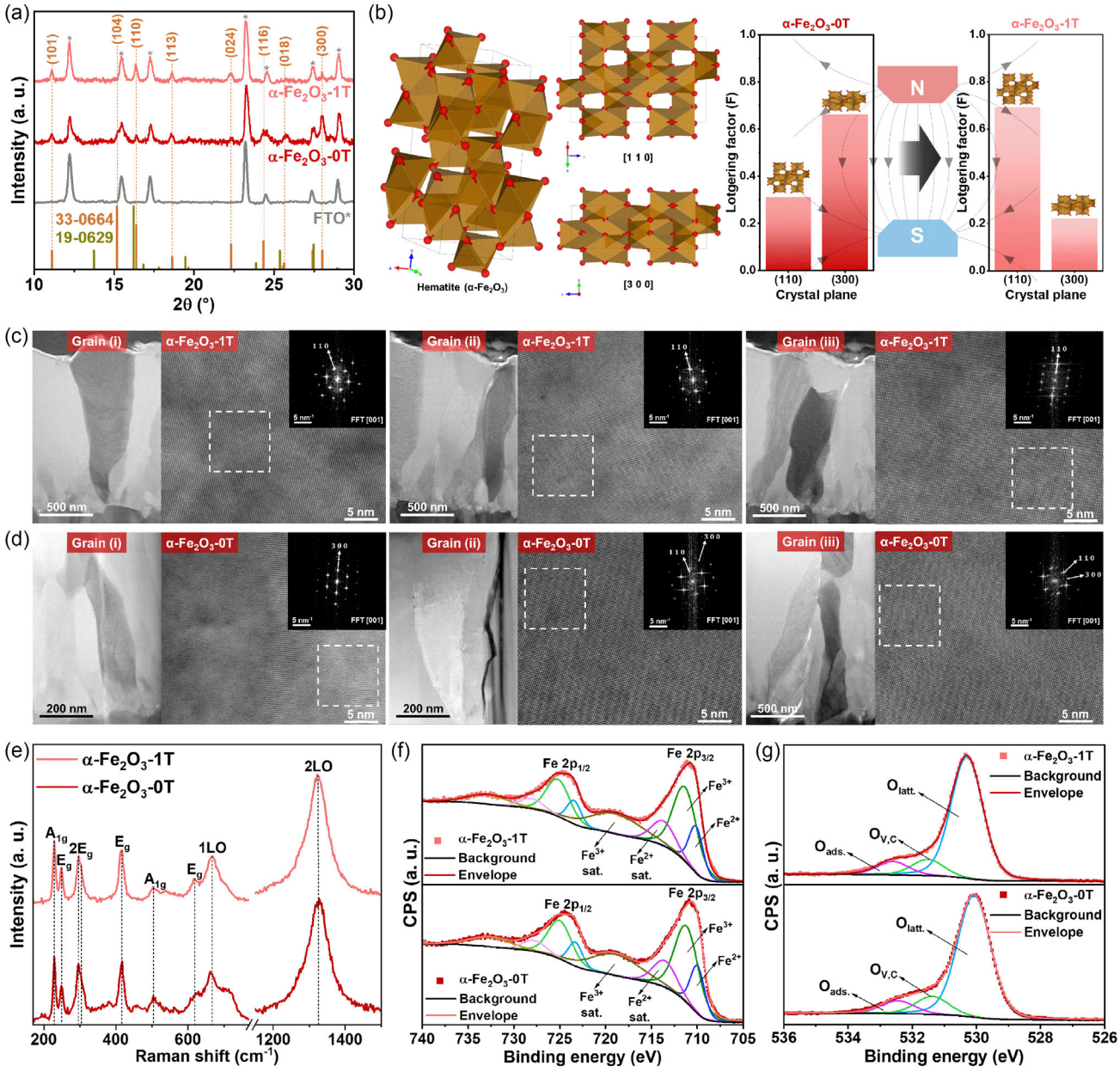

Figure 1. a) XRD patterns of FTO substrate and hematite samples grown without (α-Fe_2O_3-0 T) and with (α-Fe_2O_3-1 T) influence of an external magnetic field. Hematite (JCPDS card 33-0664) and magnetite (JCPDS card 19-0629) are displayed as references. b) Graphical representation of hematite (α-Fe_2O_3) unit cell done in VESTA software using the CIF file 9 000 139, with (110) and (300) planes highlighted. Bar graphs on the right show the degree of anisotropy change with magnetic field application. c) HRTEM images of α-Fe_2O_3-1 T with assigned crystallographic planes. d) HRTEM images of α-Fe_2O_3-0 T with assigned crystallographic planes. e) Raman spectra of α-Fe_2O_3-0 T and α-Fe_2O_3-1 T. f) Deconvoluted XPS Fe 2p high-resolution spectra of α-Fe_2O_3-0 T and α-Fe_2O_3-1 T. g) Deconvoluted XPS O 1s high-resolution spectra of α-Fe_2O_3-0 T and α-Fe_2O_3-1 T.

attributed to the presence of low oxidative energy (S2-type) surface states, which are catalytically inactive and prone to induce charge recombination in hematite polycrystalline nanostructures.[24]

The O1s high-resolution spectra for α-Fe_2O_3-0 T and α-Fe_2O_3-1 T (Figure 1g) presented three distinct oxygen species: lattice bound oxygen (530.1 eV), oxygen atoms in the vicinity of an oxygen deficient environment[25] or related to metal carbonates[26] (531.5 eV) and absorbed oxygen species (532.5 eV), the latter originating from organic moieties and moisture, due to sample exposure to air.[27] The presence of oxygen vacancies is in agreement with charge compensation effects and the existence of Fe^{2+} species on the surface of the samples. However, this assignment is controversial in the literature, and it does not rule out the presence of residual carbonated species from $Fe_2[O^tBu]_6$ precursor with matching binding energy.[25,26]

Kelvin probe force microscopy (KPFM) measurements shown in **Figure 2** provided insights into the impact of structural changes caused by mf-CVD. Overall, surface potential was reduced from ≈394 to ≈345 mV upon magnetic field influence, meaning that less potential is required to pass current through the nanostructure. This is evidence that (110) anisotropy can actively favor charge collection at the back contact. Conversely, capacitance gradient maps show common properties of multi-interfaced hematite nanostructures, with dC/dz values locally higher at the grain boundaries.[28] Interestingly, α-Fe_2O_3-1 T shows reduced capacitance gradient in both grain and boundaries, suggesting facilitated electron hopping through the grains and consequent reduction of charge recombination centers for this sample, compared to α-Fe_2O_3-0 T.

Top-view scanning electron microscopy (SEM) images displayed in Figure 2 reveal the impact of structural changes caused by mf-CVD in the surface morphology of the films. Clearly, grain growth and densification processes were altered

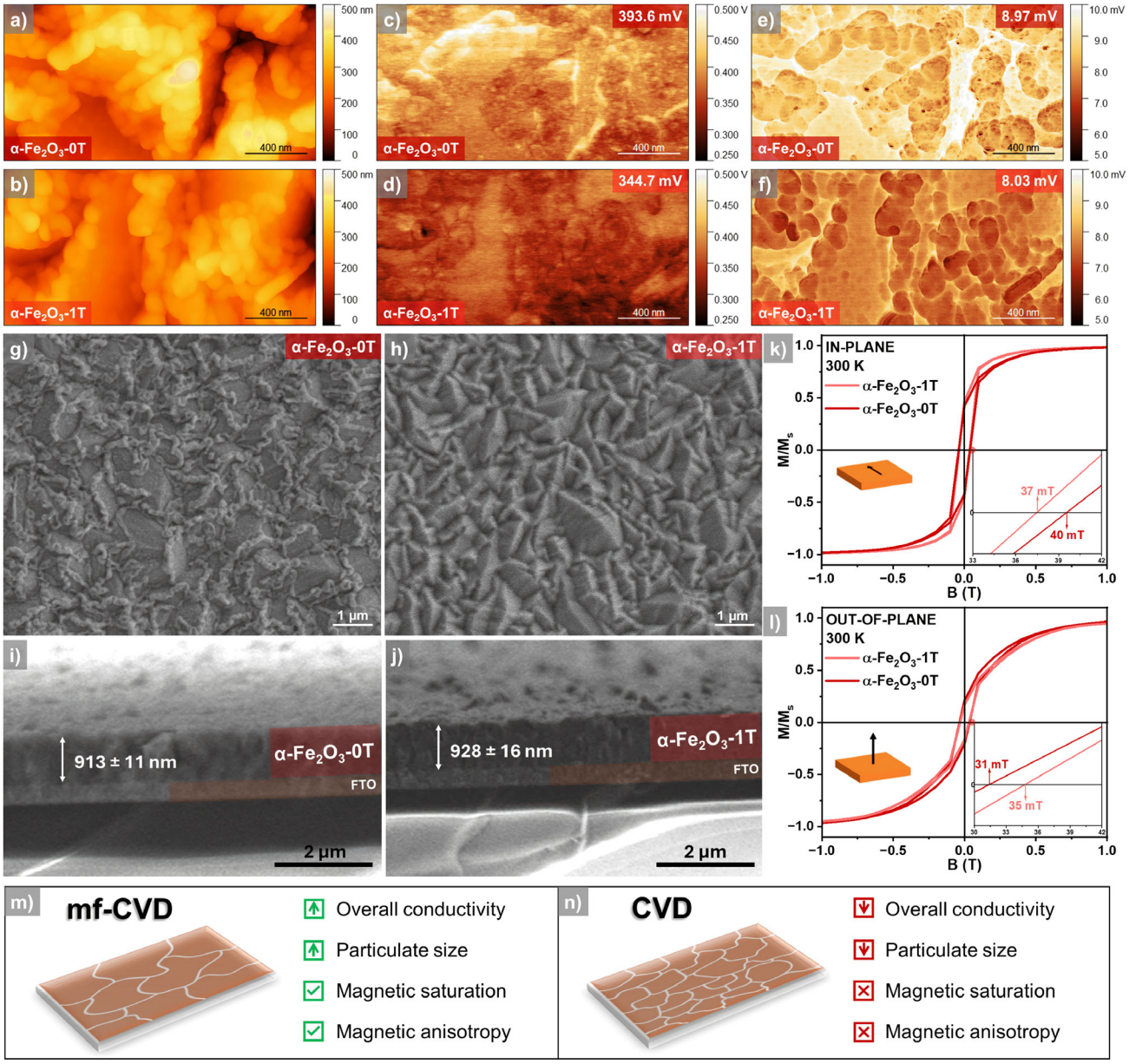

Figure 2. KPFM topographic maps of a) α-Fe_2O_3-0 T and b) α-Fe_2O_3-1 T. Surface potential maps from KPFM of c) α-Fe_2O_3-0 T and d) α-Fe_2O_3-1 T. Surface capacitance gradient (dC/dZ) maps from KPFM of e) α-Fe_2O_3-0 T and f) α-Fe_2O_3-1 T. Top-view SEM images of g) α-Fe_2O_3-0 T and h) α-Fe_2O_3-1 T. Cross-section SEM images of i) α-Fe_2O_3-0 T and j) α-Fe_2O_3-1 T, highlighting FTO substrate layers and film thicknesses. k) In-plane magnetic coercivity of α-Fe_2O_3-0 T and α-Fe_2O_3-1 T measured with a SQUID magnetometer. l) Out-of-plane magnetic coercivity of α-Fe_2O_3-0 and α-Fe_2O_3-1 T measured with a SQUID magnetometer. Schemes highlighting the properties mainly affected by m) the application of an external magnetic field during the CVD process versus n) the absence of a magnetic field, adapted from ref. [7].

by the application of the magnetic field, leading to different crystal facet exposure to the surface for α-Fe_2O_3-1 T.[7] Cross-section SEM images highlight the thickness maintenance observed for both samples, suggesting that although the magnet might change the gas-phase mechanism of precursor decomposition, the CVD process is robust enough to keep the yield of precursor used for metal oxide phase formation in the same experimental conditions.

The superconducting quantum interference device (SQUID) data revealed stronger in-plane coercivity for both samples when compared to out-of-plane measurements, despite the magnetic field applied perpendicular to the α-Fe_2O_3-1 T surface (Figure 2). The saturation of the magnetization requires large fields, more than 0.5 Tesla to reach finite remanence in both directions, although values between 30 and 40 mT are still rather large coercive fields at room temperature. This correlates with the multi-interfaced and rough morphology of CVD-grown hematite nanostructures. As there is a clear magnetic order in the samples, the preferential crystal growth changes induced by the magnetic field were responsible for inverting the in-plane and out-of-plane coercivity trends: while α-Fe_2O_3-0 T exhibited a larger in-plane coercive field, α-Fe_2O_3-1 T showed a larger out-of-plane coercive field.

Altogether, the characterization shown so far points out the drastic effect of applying an external magnetic field during CVD when using a paramagnetic precursor (see Figure 2m,n). The dynamics of gas-phase and surface reactions sensibly changed upon 1 T application, yielding out-of-plane anisotropy capable of changing long and short-range order of the nanostructures, as well as electric conductivity and magnetic saturation properties. Associated with altered crystallographic planes stacking and increased particulate size, the controlled nanostructure design observed through the mf-CVD technique changed the materials surface properties, impacting their catalytic activity.

2.2. (Photo)Electrochemical and Optical Analysis

Indeed, all structural, morphological, electrical, and magnetic changes observed by the application of a magnetic field during CVD were translated into enhanced solar water oxidation performance of α-Fe_2O_3-1 T when compared to α-Fe_2O_3-0 T. A 74% increase in photocurrent at 1.23 V_{RHE} was observed for the sample grown under magnetic field influence (**Figure 3**a), accompanied by a slightly reduced onset potential (0.89 V_{RHE} for α-Fe_2O_3-0 T and 0.85 V_{RHE} for α-Fe_2O_3-1 T) remarked in Figure 3b. It is important to highlight that from linear sweep voltammetry (LSV) measurements performed for triplicate samples (Figure 3c) and chronoamperometry (CA) analysis carried out at 1.23 V vs. RHE for 8 h (Figure S2, Supporting Information), reproducible depositions and stable hematite photoanodes, respectively, were achieved for PEC application with the CVD setup used in the experiments. This adds up to the well-known hematite reliability and stability for solar water oxidation.[29] In addition, direct optical bandgap values of ≈2.1 eV were estimated

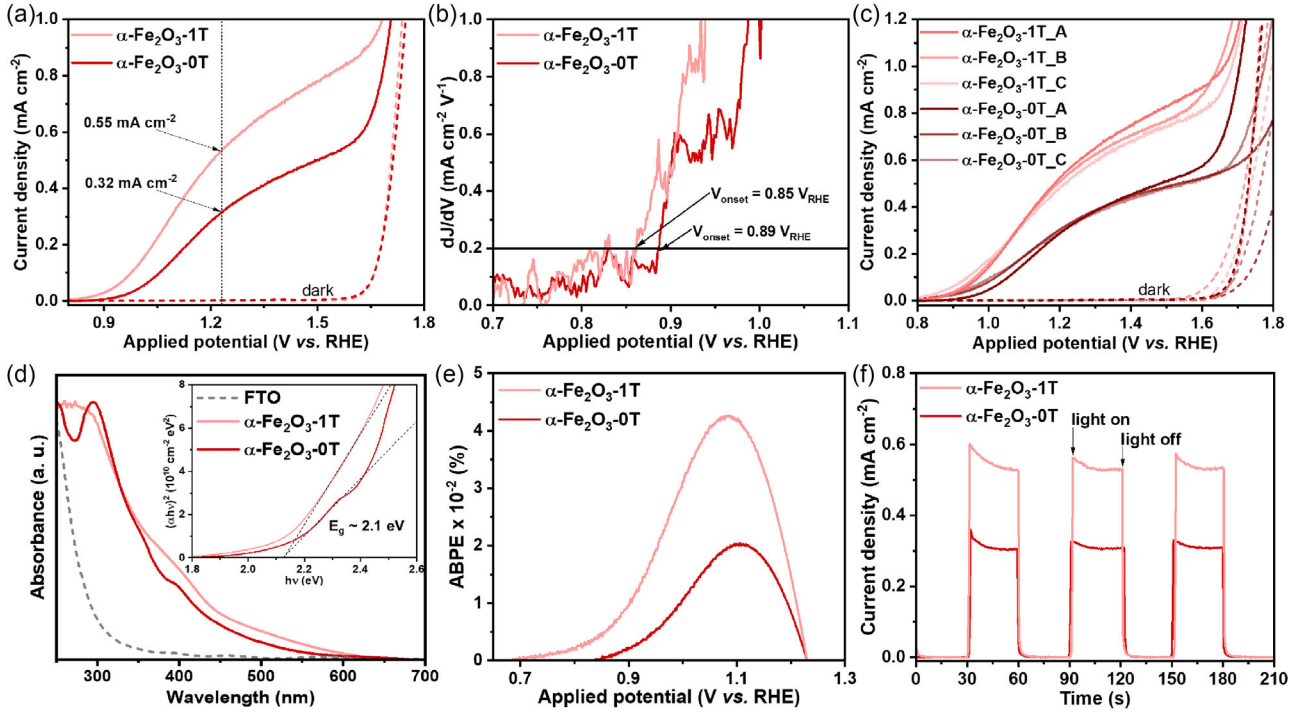

Figure 3. a) LSV curves of α-Fe_2O_3-0 and α-Fe_2O_3-1 T measured under dark conditions (dashed lines) and illumination (straight lines), highlighting the photocurrent values reached at the water oxidation thermodynamic potential (1.23 V vs. RHE). b) Estimated onset potential (V_{onset}) values for α-Fe_2O_3-0 T and α-Fe_2O_3-1 T using the first derivative of the current density (dJ/dV). c) LSV curves of triplicate samples produced with and without the influence of the magnetic field. d) Absorbance curves of FTO substrate, α-Fe_2O_3-0, and α-Fe_2O_3-1 T in the UV–vis region of the electromagnetic spectrum. Tauc plots and optical bandgap estimations for α-Fe_2O_3-0 and α-Fe_2O_3-1 T are exhibited in the inset figure. e) ABPE curves calculated for α-Fe_2O_3-0 and α-Fe_2O_3-1 T from LSV curves measured under illumination. f) Transient CA measured at 1.23 V vs. RHE under light on/light off cycles for α-Fe_2O_3-0 and α-Fe_2O_3-1 T.

from Tauc plots (Figure 3d) for both samples, assessing a common property of polycrystalline nanostructured hematite.[30]

Applied bias photon-to-current efficiency (ABPE) of α-Fe_2O_3-1 T, shown in Figure 3e, reached its maximum value of 0.043% at 1.08 V_{RHE}, while a maximum of 0.02% was reached at 1.11 V_{RHE} for α-Fe_2O_3-0 T, indicating the superior photoconversion efficiency of the sample influenced by the magnetic field, shifted to lower potentials. Furthermore, transient CA measurements (Figure 3f) exhibit anodic spikes for both samples upon switching the lamp on and off, suggesting fast charge recombination at the surface. This is attributed to the band-edge pinning effect in hematite, resulting from the accumulation of holes at surface traps and consistent with the presence of surface states acting as recombination centers.[31]

Flat band potentials determined by the Gärtner–Butler method (**Figure 4**a)[32,33] show a lower potential value for α-Fe_2O_3-1 T in contrast to α-Fe_2O_3-0 T, suggesting that the depletion layer formation in α-Fe_2O_3-1 T can happen at smaller voltages, favoring PEC activity.[34,35] Charge separation efficiency (η_{sep}) curves calculated from LSV measurements in the presence of H_2O_2 hole scavenger (see Figure S3, Supporting Information) and J_{abs} values (Table S3, Supporting Information) corroborate the assumption of better charge transport through the (110) planes for α-Fe_2O_3-1 T, as an increase in magnetic anisotropy in this crystallographic direction enhanced this parameter in comparison to α-Fe_2O_3-0 T (Figure 4b). Charge transfer efficiency (η_{tr}) curves (Figure 4c), also extracted from measurements with a hole scavenger, hint that the enhanced charge injection for α-Fe_2O_3-1 T, in contrast to α-Fe_2O_3-0 T, might be due to the reduced number of surface states in the magnetically altered sample. Conversely, enhanced photovoltage measured at open circuit potential (OCP) conditions from 155 mV for α-Fe_2O_3-0 T to 188 mV for α-Fe_2O_3-1 T (Figure 4d) is evidence of a stronger built-in electric field for the nanostructure influenced by the magnetic field (see full OCP measurements in Figure S4, Supporting Information).[36,37] This is further assumed as charge tends to recombine faster (3.7 s) for α-Fe_2O_3-1 T in the absence of the illumination-induced built-in electric field, in contrast to 8.6 s for α-Fe_2O_3-0 T (Figure 4e).

Additionally, double capacitance (C_{dl}) values shown in Figure 4f were calculated from cyclic voltammetry (CV) measurements performed at different scan rates in a nonfaradaic region for α-Fe_2O_3-0 T and α-Fe_2O_3-1 T (see Figure S5, Supporting Information). This result highlights that the application of a magnetic field during CVD induces both structural and surface morphological refinement, yielding α-Fe_2O_3 nanostructures with enhanced electrochemically active surface area (ECSA). The ECSA increases from 46.5 for α-Fe_2O_3-0 T to 49.8 for α-Fe_2O_3-1 T, contributing directly to the improved water oxidation performance observed in the magnetically structured film (Figure 3 and 4).

For advanced insights into the origin of the enhanced photoresponse of α-Fe_2O_3-1 T, electrochemical impedance spectroscopy (EIS) experiments (**Figure 5**) were performed in the same potential range as the previous analysis, and the data were interpreted using an equivalent circuit model shown as an inset

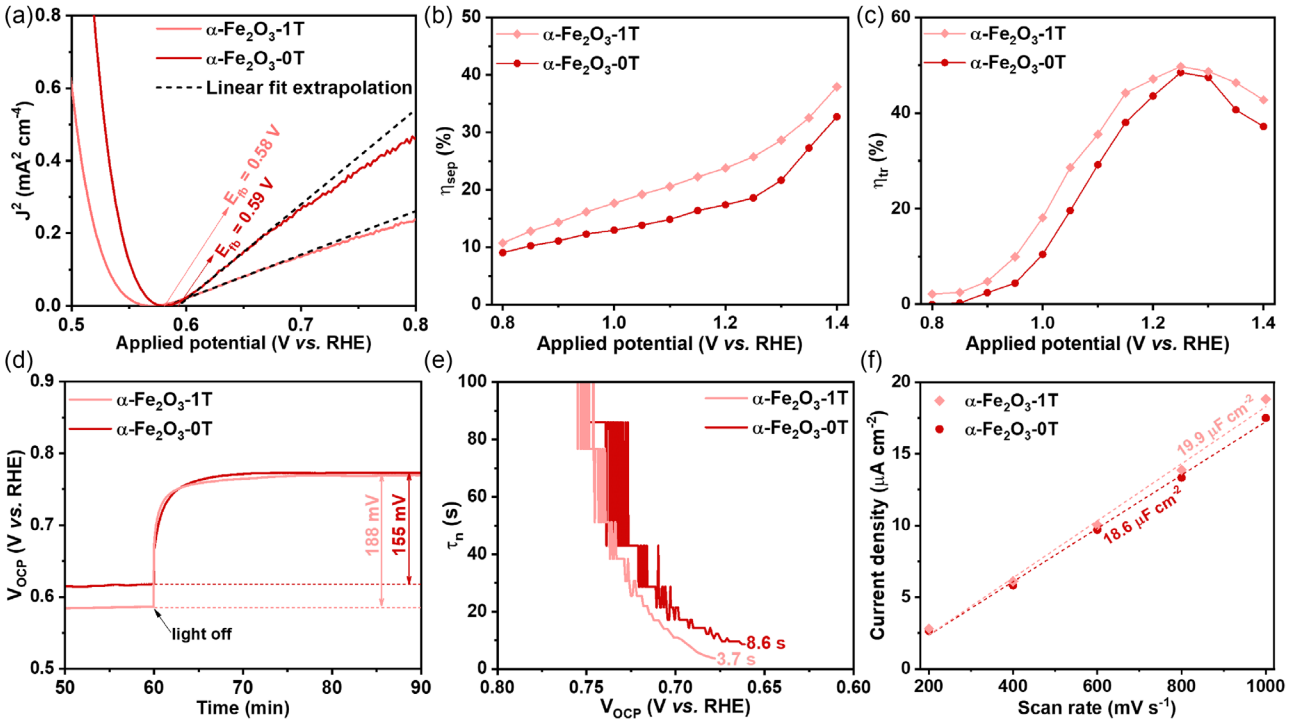

Figure 4. a) Flat band potential (E_{fb}) estimations for α-Fe_2O_3-0 T and α-Fe_2O_3-1 T according to the Gartner–Butler method. b) Charge separation efficiency (η_{sep}) values calculated for α-Fe_2O_3-0 T and α-Fe_2O_3-1 T from measurements with H_2O_2 hole scavenger. c) Charge transfer efficiency (η_{tr}) values calculated for α-Fe_2O_3-0 T and α-Fe_2O_3-1 T from measurements with H_2O_2 hole scavenger. d) Transient OCP curves of α-Fe_2O_3-0 T and α-Fe_2O_3-1 T, highlighting the photovoltages generated by the photoanodes. e) Estimated electron lifetime (τ_n) values for α-Fe_2O_3-0 and α-Fe_2O_3-1 T calculated from OCP measurements. f) Current density versus scan rate plots for CV measurements performed at nonfaradaic regions for α-Fe_2O_3-0 and α-Fe_2O_3-1 T.

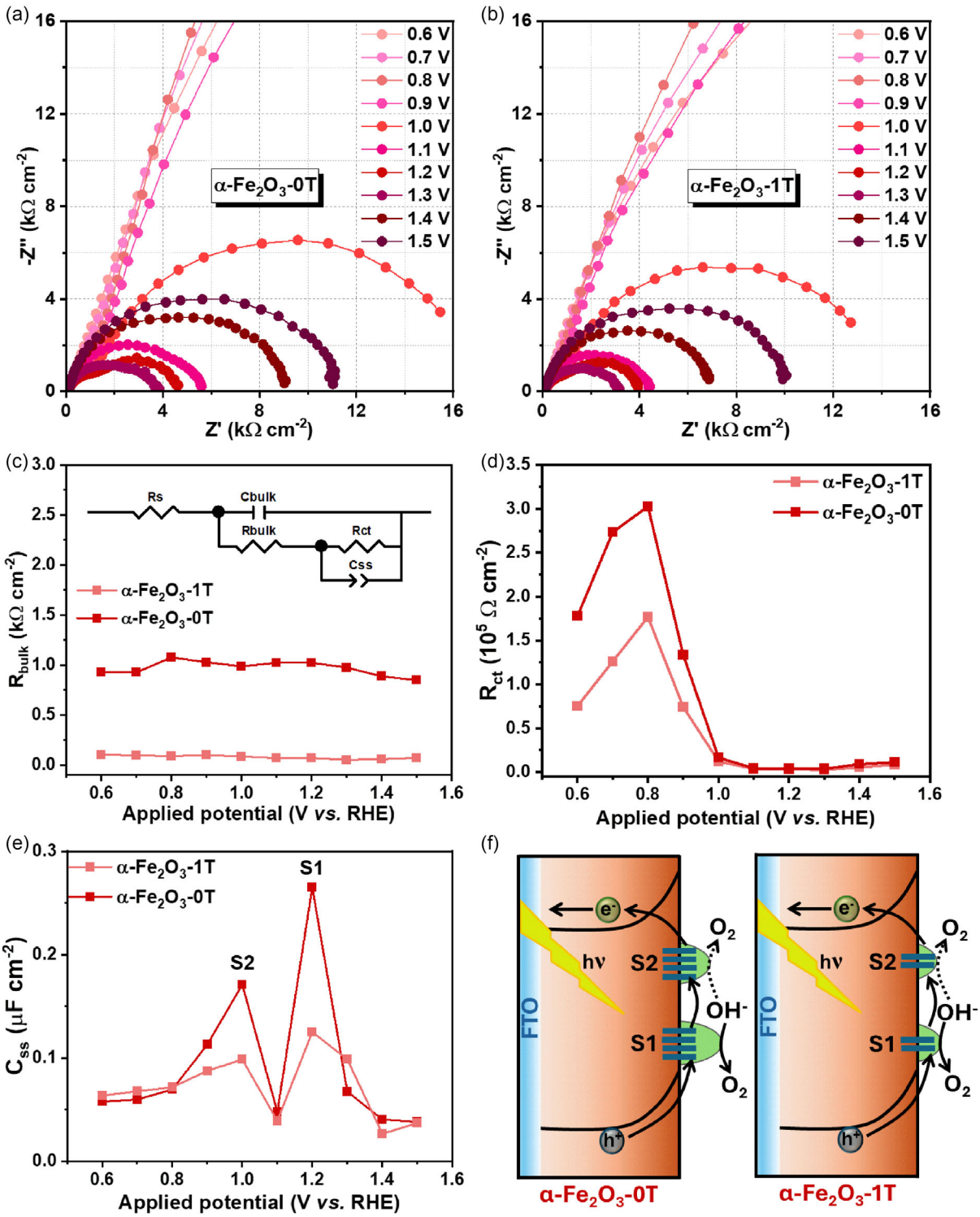

Figure 5. Nyquist plots of EIS data measured under simulated sunlight illumination (100 mW cm^{-2}) for a) α-Fe_2O_3-0 T and b) α-Fe_2O_3-1 T. c) Plot of resistance values from EIS in the 0.6 - 1.5 V_{RHE} range representing hole migration to the surface and trapping at surface states (R_{bulk}) for α-Fe_2O_3-0 and α-Fe_2O_3-1 T. The equivalent circuit chosen for data fitting is shown in the inset picture. d) Plot of resistance values from EIS in the 0.6–1.5 V_{RHE} range assigned as charge transfer resistance to the electrolyte with surface states considered (R_{ct}) for α-Fe_2O_3-0 T and α-Fe_2O_3-1 T. e) Plot of capacitance values from EIS in the 0.6–1.5 V_{RHE} range ascribed to charge transfer to the electrolyte in the presence of surface states (C_{ss}) for α-Fe_2O_3-0 and α-Fe_2O_3-1 T. f) Schematic representation of solar water oxidation catalyzed by α-Fe_2O_3-0 T (left) and α-Fe_2O_3-1 T (right), indicating the reduced amount of surface states for the latter sample. The scheme also represents the role of surface states (S1 and S2) as intermediates in the water oxidation mechanism of hematite.

in Figure 5c. Space-charge capacitances for hematite bulk (C_{bulk}) and charge transfer to the electrolyte in the presence of surface states (C_{ss}) were considered, respectively, and resistance components representing the circuit series resistances on FTO/α-Fe_2O_3 and the electrolyte (R_s), the resistance accounting for hole migration to the surface and trapping at surface states (R_{bulk}), and charge transfer resistance to the electrolyte with surface states considered (R_{ct}).[38,39] A constant phase element was used to represent C_{ss}, and its coefficient was kept around 0.7–0.9 for better approximation to a conventional capacitor. Nyquist plots for α-Fe_2O_3-0 T and α-Fe_2O_3-1 T are shown in Figure 5, and fitting parameters are displayed in Table S4 and S5, Supporting Information.

It was noted that resistance values due to hole migration to the surface and trapping at surface states (R_{bulk}) were somehow constant for both samples throughout the potential range analyzed (Figure 5c), but R_{bulk} values calculated for α-Fe_2O_3-1 T were almost ten times lower than those found for α-Fe_2O_3-0 T. This agrees with the charge separation efficiency (η_{sep}) values calculated at the depletion layer in the presence of a hole scavenger (Figure 4b), which indicated superior charge mobility for α-Fe_2O_3-1 T. Conversely, charge transfer resistance (R_{ct}) values (Figure 5d) are considerably high for both samples at lower potentials ($V < 1.0\ V_{RHE}$), corroborating the low or negligible currents generated in this potential range shown by LSV measurements (Figure 3a). However, R_{ct} values are close to zero at $V > 1.0\ V_{RHE}$, suggesting these potentials successfully promote charge injection to the electrolyte. This is particularly interesting in comparison to η_{tr} values obtained from LSV measurements performed with a hole scavenger (Figure 4c) because charge injection to the electrolyte starts to have considerable values after 1.0 V_{RHE}, as R_{ct} from EIS drastically decreases (Figure 5d).

The capacitances related to charge transfer to the electrolyte in the presence of surface states (C_{ss}) show the considerable presence of surface states around 1.0 V_{RHE} and later at 1.2 V_{RHE} (Figure 5e). These surface states are commonly assigned as S2 and S1, respectively.[39,40] S1-type surface states require higher energies to be activated and are referenced to mediate the solar water oxidation mechanism in hematite.[40] Although S2-type surface states are usually said to be inactive or act as recombination sites, recent studies show that they can also actively intermediate water oxidation, requiring less energy to be activated.[39,40] Figure 5f summarizes the role of both surface state types for polycrystalline nanostructured hematite. For the samples studied in this work, the possibility of S2-type surface states acting in the water oxidation cannot be excluded, as photocurrent is generated at 1.0 V_{RHE}, but additional studies are needed to fully understand their role during PEC operation.

Calculated C_{ss} values for α-Fe_2O_3-1 T are lower than the values found for α-Fe_2O_3-0 T in the potential range analyzed. From lower R_{bulk} and R_{ct} values obtained for α-Fe_2O_3-1 T, one should expect that a major quantity of holes would successfully reach the surface of the semiconductor, increasing C_{ss} values. However, higher charge transfer efficiency (η_{tr}) shown in Figure 4c and increased ECSA of α-Fe_2O_3-1 T in contrast to α-Fe_2O_3-0 T (Figure 4f) are good indicatives of comparatively lower amount of surface states for α-Fe_2O_3-1 T, and faster water oxidation kinetics for this sample, respectively. Moreover, enhanced photovoltage (V_{ph}) generated for α-Fe_2O_3-1 T (Figure 4d) reduces the overpotential necessary for water oxidation, accelerating reaction rates. These results corroborate the reduced C_{ss} observed for α-Fe_2O_3-1 T, as hole accumulation at the surface is expected to be less pronounced than in α-Fe_2O_3-0 T. The surface state density (N_{ss}) was calculated using the C_{ss} values obtained from EIS at the semiconductor–electrolyte interface using the formula: $N_{ss} = C_{ss}/q$, where q represents the electron charge (1.602×10^{-19} C).[41] As shown in Figure S6, Supporting Information, the N_{ss} values of α-Fe_2O_3-1 T are smaller than the values calculated for α-Fe_2O_3-0 T, corroborating lower charge density accumulation at the surface states of α-Fe_2O_3-1 T.

In summary, applying a 1 T magnetic field during deposition induced preferential [110] crystallographic orientation, larger crystallites, and reduced structural disorder due to spin polarization, which enhanced electron transport to the back contact, improved charge separation/collection, and lowered interfacial energies that hinder electron hopping. EIS confirmed reduced bulk resistance in α-Fe_2O_3-1 T versus α-Fe_2O_3-0 T, reflecting mitigated charge transport limitations, stronger built-in electric field (supported by OCP), and more efficient charge injection. Magnetic-field-induced anisotropy and densification further decreased surface potential and capacitance gradients (as seen in KPFM), exposed distinct crystal facets with (110) orientation to the electrolyte, increased ECSA, and reduced surface state density (observed by EIS), leading to higher charge transfer efficiency and lower charge accumulation/recombination at the surface, as verified by smaller C_{ss} values. Collectively, these bulk and surface structural refinements delivered a 74% increase in photoresponse for the magnetically altered material. Future studies are needed to clearly elucidate the mechanistic changes in water oxidation provoked by mf-CVD, as the OER mechanism remains under active debate.[42–44]

Furthermore, an extended stability test was conducted for α-Fe_2O_3-1 T using a system with refluxed electrolyte feeding to assess its viability for application in PEC devices (**Figure 6**a). The material showed remarkable stability for 100 h of operation, showcasing the system as a promising model candidate for photoelectrolyzers when compared to similar anisotropic systems (Table S6, Supporting Information). The surface composition and morphological features of α-Fe_2O_3-1 T were systematically analyzed using XPS and SEM, respectively, after the long-term stability test. Figure 6b–d, S7, and Table S7,S8, Supporting Information, show the maintenance of surface properties, which are well documented in the literature for hematite.[28,30] Furthermore, an increased adsorbed oxygenated species (O_{ads}) percentage was observed for α-Fe_2O_3-1 T in the O 1s high-resolution XPS spectra after OER (Table S9 and S10, Supporting Information). This is attributed to surface hydroxylation in a strongly alkaline medium after long PEC operation.[27] Also, the increased intensity in the $O_{V,C}$ component reinforces the hypothesis that carbonate adsorbates are contributing to this signal. The amount of gas evolution, quantified by gas chromatography (Figure 6e,f), also demonstrates the structural and chemical stability of the photoanodes, as the high faradaic efficiency values observed for both α-Fe_2O_3-0 T and α-Fe_2O_3-1 T are evidence that nearly all the photogenerated charge is used to drive the overall water splitting reaction.

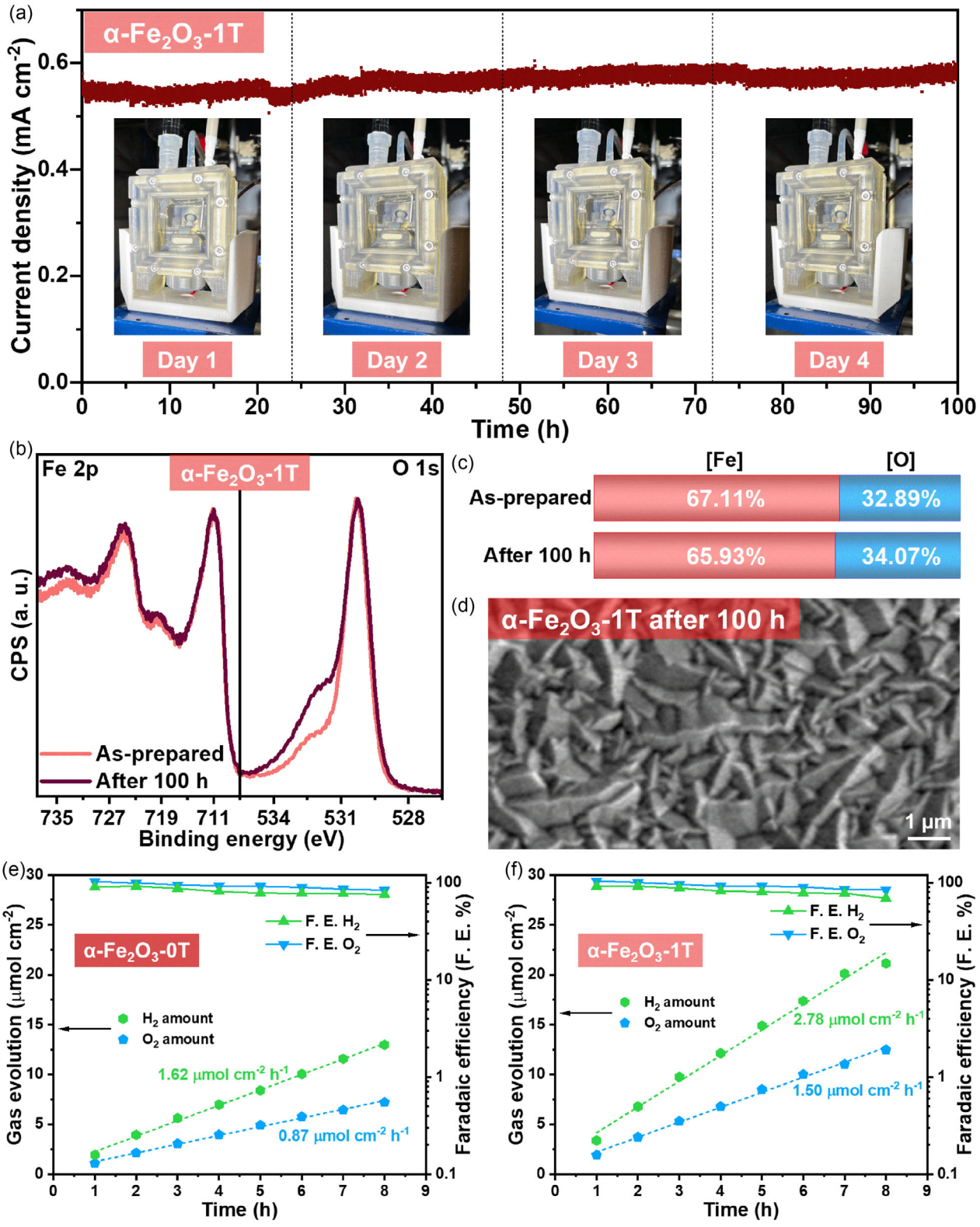

Figure 6. a) CA measurement for PEC operation of α-Fe_2O_3-1 T for 100 h. Inset figures show pictures of the system with refluxed electrolyte feeding. b) Normalized XPS Fe 2p and O 1s high-resolution spectra of α-Fe_2O_3-1 T as-prepared and after PEC operation for 100 h. c) Iron/oxygen ratio at the surface of α-Fe_2O_3-1 T as-prepared and after 100 h operation extracted from XPS survey spectra. d) Top-view SEM image of α-Fe_2O_3-1 T after 100 h. Amounts of generated gases measured by gas chromatography for e) α-Fe_2O_3-0 T and f) α-Fe_2O_3-1 T.

3. Conclusion

This study highlighted mf-CVD as an effective and scalable strategy for tailoring the crystallographic orientation, morphology, and electronic properties of hematite (α-Fe_2O_3) thin films. The application of a magnetic field (1 T) during deposition induced preferential crystal growth along the [110] direction, reduced structural disorder, and enhanced electrical conductivity. These structural modifications led to a surface morphology that significantly favored the PEC performance of the materials. The α-Fe_2O_3-1 T photoanode exhibited a 74% increase in photocurrent density at 1.23 V vs. RHE compared to α-Fe_2O_3-0 T, along with improved charge separation and transfer efficiencies, greater photovoltage, and increased electrochemically active surface area. Moreover, EIS further confirmed a reduced density of surface states for the sample grown under field influence, underscoring the role of mf-CVD in modulating interfacial charge dynamics. Furthermore, the magnetically altered sample showed remarkable stability for 100 h of PEC operation. Collectively, these findings demonstrate the efficacy of mf-CVD as a powerful tool for engineering metal oxide semiconductors, hinting its potential application for a broad range of materials spanning renewable energy conversion technologies.

4. Experimental Section

Substrate Preparation: Glass-coated fluorine-doped tin oxide (FTO) purchased from Ossila (1 mm thick, 25×25 mm) were cut into 8.3×12.5 mm pieces. Substrate cleaning was done by ultrasonication in 10% v/v Hellmanex aqueous solution, deionized water, isopropanol, and acetone for 15 min each, in this order. Before changing the cleaning solvent, substrates were rinsed with the subsequent solvent. No additional surface treatment was performed.

Film Deposition: The gas-phase deposition of iron oxide layers was performed using iron *tert*-butoxide ($Fe_2[O^tBu]_6$), synthesized as previously reported,[14] as precursor in a horizontal cold-wall magnetic field-assisted chemical vapor deposition (mf-CVD) reactor. The precursor temperature was kept constant at 110 °C to ensure a homogeneous gas flow. Prior to deposition, the reactor was evacuated to 3×10^{-5} mbar. The precursor flux was guided over a DC joule-heated FTO substrate (550 °C). Deposition time was kept constant at 10 min, and the experiments were performed without or under the influence of an external magnetic field ($\vec{B} = 1$ T). Samples were annealed after deposition for 60 min at 550 °C under an air atmosphere in the mf-CVD vented reactor.

Materials Characterization: Thin film XRD patterns were measured using a Stoe Stadi-MP equipped with a Dectris Mythen 1 K detector and performed in Bragg–Brentano geometry using a Mo-K_α ($\lambda = 0.07094$ nm) source. Surface chemical composition of the photoanodes was investigated by XPS using an ESCA *M*-Probe spectrometer from Surface Science Instruments equipped with a monochromatic K_α-Al source ($h\nu = 1486.6$ eV). Adventitious carbon (C–C/C–H) at 284.8 eV was used to calibrate the XPS spectra, and data analysis was performed using a Gaussian–Lorentzian function GL(30) with Shirley-type background subtraction (CasaXPS software). For post-mortem analysis after 100 h of PEC operation, the sample was rinsed with deionized water and dried in air before XPS measurements. Raman spectroscopy measurements were performed at room temperature (293 K) on a Witec Raman Rise instrument with a 532 nm laser. KPFM measurements were performed in an NX-10 Park Systems microscope, with a NanoSensors Pt/Ir-coated silicon probe, PPP-EFM model. Top-view and cross-section morphologies were analyzed using a Zeiss Sigma 300 VP Rise field emission scanning electron microscope, operated at 5 kV. HRTEM analysis was carried out in a TEM model FEI Titan Cubed Themis aberration-corrected microscope operating at 300 kV. Magnetization properties were investigated by a Quantum Design MPMS3 SQUID magnetometer at 300 K. Absorbance measurements in the UV–vis region were done with a Perkin Elmer Lambda 950 spectrometer from 200 to 700 nm.

(Photo)Electrochemical Measurements: The hematite films were assembled as photoanodes for water oxidation in a three-electrode electrochemical cell containing a platinum counter electrode, Ag/AgCl (KCl 3M) reference electrode, and 1.0 mol L^{-1} KOH (Fisher Scientific, $\geq$85%) electrolyte solution (pH = 13.6). The area of the photoanodes measured in this configuration was 0.36 cm^2. Using a VersaSTAT4 Potentiostat/Galvanostat (Princeton Applied Research), measurements were conducted under sunlight illumination (100 Mw cm^{-2}) simulated by a 450 W Xe lamp (Osram, ozone-free) equipped with an AM 1.5 Global filter. The power (1 sun) was adjusted and calibrated to the position of the photoanodes with the aid of a certified reference solar cell (RR-1001, Rera Solutions). LSV measurements were done from −0.7 to 0.9 V against the reference electrode at a scan rate of 50 mV s^{-1} under dark and light conditions. LSV was also done adding, H_2O_2 0.5M in the electrolyte as a hole scavenger. CA analysis was carried out under chopped illumination for 210 and 30 s light on/light off intervals, and under continuous illumination for 8 h. Extended stability test was done for α-Fe_2O_3-1 T up to 100 h. Transient OCP measurements were performed for 90 min, with 30 min stabilization (dark condition), 30 min under illumination, and 30 min after with light off. CV at different scan rates (200, 400, 600, 800, and 1000 mV s^{-1}) was measured in a 0.1 V potential window around the OCP values of the samples for ECSA determination. EIS was carried out from 10 kHz to 0.1 Hz, with an amplitude of 0.01 V RMS and 10 points per decade. Gas products were quantified by gas chromatography (GC System 7890B Agilent Technologies equipped with a thermal conductivity detector – TCD), using Ar as carrier gas. GC data were extracted from the software Agilent OpenLab CDS. Further details on calculations can be found in the Supporting Information (SI) file. All potentials were converted to RHE using the Nernst Equation (1)

$$E_{RHE} = E_{Ag/AgCl} + E^0_{Ag/AgCl} + 0.059\,pH \quad (1)$$

Supporting Information

Supporting Information is available from the Wiley Online Library or from the author.

Acknowledgements

The authors acknowledge the support given by the São Paulo Research Foundation (FAPESP) through the grant 2024/05567-3; the Research, Innovation and Dissemination Center for Molecular Engineering for Advanced Materials - CEMol (FAPESP grant 2024/00989-7); the University of Cologne and the German Science Foundation - DFG. The authors thank Jörg Schöpf for measurements with a SQUID magnetometer and Cleyton A. Biffe for KPFM measurements.

Open Access funding enabled and organized by Projekt DEAL.

Conflict of Interest

The authors declare no conflict of interest.

Data Availability Statement

The data that support the findings of this study are available from the corresponding author upon reasonable request.

Keywords

green hydrogen, hematite, iron *tert*-butoxide, magnetic field-assisted chemical vapor deposition, nanostructure tailoring

Received: July 25, 2025
Revised: September 24, 2025
Published online:

[1] L. Sun, G. Yuan, L. Gao, J. Yang, M. Chhowalla, M. H. Gharahcheshmeh, K. K. Gleason, Y. S. Choi, B. H. Hong, Z. Liu, *Nat. Rev. Methods Primers* **2021**, *1*, 5.
[2] A. H. Choolakkal, P. Niiranen, S. Dorri, J. Birch, H. Pedersen, *Nat. Commun.* **2024**, *15*, 10667.
[3] Z. Wu, Y. Zhang, Y. Shen, W. Zhang, G. Shao, *Adv. Mater. Interfaces* **2020**, *7*, 2000854.
[4] D. Wei, Y. Liu, L. Cao, L. Fu, X. Li, Y. Wang, G. Yu, *J. Am. Chem. Soc.* **2007**, *129*, 7364.
[5] B. Singh, T. Fischer, S. Mathur, *J. Mater. Chem. A* **2025**, *13*, 20104.
[6] M. Pyeon, V. Rauch, D. Stadler, M. Gürsoy, M. Deo, Y. Gönüllü, T. Fischer, T. Hwang, S. Mathur, *Adv. Eng. Mater.* **2019**, *21*, 1.
[7] D. Stadler, D. N. Mueller, T. Brede, T. Duchoň, T. Fischer, A. Sarkar, M. Giesen, C. M. Schneider, C. A. Volkert, S. Mathur, *J. Phys. Chem. Lett.* **2019**, *10*, 6253.
[8] D. Stadler, T. Brede, D. Schwarzbach, F. Maccari, T. Fischer, O. Gutfleisch, C. A. Volkert, S. Mathur, *Nanoscale Adv.* **2019**, *1*, 4290.
[9] A. Raauf, J. Leduc, M. Frank, D. Stadler, D. Graf, M. Wilhelm, M. Grosch, S. Mathur, *Inorg. Chem.* **2021**, *60*, 1915.
[10] H. Lee, Z. T. Aytuna, A. Bhardwaj, M. Wilhelm, L. Khan, B. May, D. N. Mueller, S. Mathur, *Adv. Eng. Mater.* **2023**, *25*, 2.
[11] P. Tutacz, D. Stadler, T. Karimpour, T. Duchoň, S. Cramm, C. M. Schneider, T. Fischer, D. N. Mueller, S. Mathur, *Chem. Mater.* **2023**, *35*, 8050.
[12] D. Barreca, G. Carraro, A. Gasparotto, C. Maccato, C. Sada, A. P. Singh, S. Mathur, A. Mettenbörger, E. Bontempi, L. E. Depero, *Int. J. Hydrogen Energy* **2013**, *38*, 14189.
[13] A. Mettenbörger, T. Singh, A. P. Singh, T. T. Järvi, M. Moseler, M. Valldor, S. Mathur, *Int. J. Hydrogen Energy* **2014**, *39*, 4828.
[14] S. Mathur, M. Veith, V. Sivakov, H. Shen, V. Huch, U. Hartmann, H. B. Gao, *Chem. Vap. Deposition* **2002**, *8*, 277.
[15] S. Kment, P. Schmuki, Z. Hubicka, L. Machala, R. Kirchgeorg, N. Liu, L. Wang, K. Lee, J. Olejnicek, M. Cada, I. Gregora, R. Zboril, *ACS Nano* **2015**, *9*, 7113.
[16] J. Talibawo, J. S. Nyarige, P. I. Kyesmen, M. C. Cyulinyana, M. Diale, *Mater. Res. Express* **2022**, *9*, 026401.
[17] M. Marelli, A. Naldoni, A. Minguzzi, M. Allieta, T. Virgili, G. Scavia, S. Recchia, R. Psaro, V. Dal Santo, *ACS Appl. Mater. Interfaces* **2014**, *6*, 11997.
[18] K. C. Bedin, B. Mouriño, I. Rodríguez-Gutiérrez, J. B. Souza Junior, G. T. G. T. dos Santos, J. Bettini, C. A. R. Costa, L. Vayssieres, F. L. Souza, *Chin. J Catal.* **2022**, *43*, 1247.
[19] J. Redondo, J. Michalička, F. Kraushofer, G. Franceschi, B. Šmid, N. Kumar, O. Man, M. Blatnik, D. Wrana, B. Mallada, M. Švec, G. S. Parkinson, M. Setvin, M. Riva, U. Diebold, J. Čechal, *Adv. Mater. Interfaces* **2023**, *10*, 2300602.
[20] S. P. Porto, R. S. Krishnan, *J. Chem. Phys.* **1967**, *47*, 1009.
[21] C. P. Marshall, W. J. Dufresne, C. J. Ru fledt, *J. Raman Spectrosc.* **2020**, *51*, 1522.
[22] K. T. Thomaz, K. C. Bedin, I. Rodríguez-Gutiérrez, N. C. Verissimo, J. Bettini, F. L. Souza, *Mater. Today Energy* **2023**, *37*, 101399.
[23] A. P. Grosvenor, B. A. Kobe, M. C. Biesinger, N. S. McIntyre, *Surf. Interface Anal.* **2004**, *36*, 1564.
[24] J. Li, H. Chen, C. A. Triana, G. R. Patzke, *Angew. Chem.* **2021**, *133*, 18528.
[25] T. J. Frankcombe, Y. Liu, *Chem. Mater.* **2023**, *35*, 5468.
[26] F. E. Zengotita, N. Lahiri, M. H. Engelhard, M. Zhukovskyi, M. R. Vejar, K. M. Rosso, C. I. Pearce, A. E. Hixon, *J. Phys. Chem. C* **2025**, *129*, 7316.
[27] A. S. M. Ismail, I. Garcia-Torregrosa, J. C. Vollenbroek, L. Folkertsma, J. G. Bomer, T. Haarman, M. Ghiasi, M. Schellhorn, M. Nachtegaal, M. Odijk, A. van den Berg, B. M. Weckhuysen, F. M. F. de Groot, *ACS Catal.* **2021**, *11*, 12324.
[28] N. C. Verissimo, F. A. Pires, I. Rodríguez-Gutiérrez, J. Bettini, T. E. R. Fiuza, C. A. Biffe, F. E. Montoro, G. R. Schleder, R. H. R. Castro, E. R. Leite, F. L. Souza, *J. Mater. Chem. A* **2024**, *12*, 6280.
[29] T. H. Jeon, G. Hee Moon, H. Park, W. Choi, *Nano Energy* **2017**, *39*, 211.
[30] F. A. Pires, G. T. dos Santos, J. Bettini, C. A. R. Costa, R. V. Gonçalves, R. H. R. Castro, F. L. Souza, *Sustainable Energy Fuels* **2023**, *7*, 5005.
[31] Q. Zhao, P. Huang, D. Hu, T. B. Li, B. Xu, *ChemPhotoChem* **2023**, *7*, e202300013.
[32] W. W. Gärtner, *Phys. Rev.* **1959**, *116*, 84.
[33] M. A. Butler, *J. Appl. Phys.* **1977**, *48*, 1914.
[34] A. Hankin, F. E. Bedoya-Lora, J. C. Alexander, A. Regoutz, G. H. Kelsall, *J. Mater. Chem. A* **2019**, *7*, 26162.
[35] J Su, J. Zhang, S. Chai, Y. Wang, S. Wang, Y. Fang, *Acta Phys. -Chim. Sin.* **2024**, *40*, 2408012.
[36] S.-Y. Yuan, L.-W. Jiang, J.-S. Hu, H. Liu, J.-J. Wang, *Nano Lett.* **2023**, *23*, 2354.
[37] C Xu, H. Wang, H. Guo, K. Liang, Y. Zhang, W. Li, J. Chen, J. S. Lee, H. Zhang, *Nat. Commun.* **2024**, *15*, 9712.
[38] K. C. Bedin, I. Rodríguez-Gutiérrez, L. R. Peregrino, L. Vayssieres, F. L. Souza, *J. Am. Ceram. Soc.* **2023**, *106*, 79.
[39] Z. Pan, S. Chen, K. Katayama, *J. Phys. Chem. C* **2023**, *127*, 3904.
[40] J. Li, W. Wan, C. A. Triana, H. Chen, Y. Zhao, C. K. Mavrokefalos, G. R. Patzke, *Nat. Commun.* **2021**, *12*, 1.
[41] X. Long, J. Wei, C. Shen, Q. Gao, X. Zhao, *Langmuir* **2025**, *41*, 7429.
[42] Y. Wang, J. Zhang, X. Wu, S. Wang, M. Anpo, Y. Fang, *Chin. Chem. Lett.* **2025**, *36*, 110439.
[43] S. Xu, J. Yang, P. Su, Q. Wang, X. Yang, Z. Zhou, Y. Li, *Nat. Commun.* **2024**, *15*, 10411.
[44] Y.-P. Zhao, G.-P. Yi, W. Yu, T. H. Tao, P.-Y. Tang, *J. Phys. Chem. C* **2025**, *129*, 3.